

Empirical mode Decomposition and Dual Sigmoid Activation Function-Based Faster RCNN for Big Data Doppler Scan Image Classification

S. Sandhya Kumari¹, Dr.K.Sandhya Rani²

¹Research Scholar, Dept. of Computer Science, SPMVV, Tirupati, India

²Professor, Dept. of Computer Science, SPMVV, Tirupati, India

Email : sridharamsandhya@gmail.com, sandhyaranikasireddy@yahoo.co.in

Available online at: <https://www.ijcert.org/>

Received: 14/09/2021,

Revised: 19/09/ 2021,

Accepted: 28/09/2021,

Published: 03/10/2021

Abstract: - This paper proposes a big data Doppler scan image classification system that uses empirical mode decomposition (EMD) and dual sigmoid activation function-based faster region convolutional neural network (RCNN). This approach initially arranges the pixels of the Doppler scan images in a zig-zag order sequence. This one-dimensional sequence is decomposed to L number of intrinsic mode function (IMF) using the EMD algorithm. The spectrums of the decomposed IMF are estimated using the one-dimensional Fourier transforms. Required IMFs are then selected based on the frequency spacing estimated on the Fourier spectrum. The resultant image is then reconstructed using the selected IMF's. The resultant Doppler scan image has less redundant information and is trained using a faster RCNN algorithm. Instead of using the traditional activation functions, the proposed faster RCNN uses a dual sigmoid activation function that classifies the Doppler images into five classes. The classes are namely Maternal cervix, Thorax, Femur, Brain, Abdomen, and other regions. The experimental evaluation uses the parameters namely F1 score, specificity, accuracy, sensitivity, precision, and time complexity with the big data Doppler ultrasound scan image dataset that contains 12400 images collected from 1792 patients.

Keywords: Doppler scan, Empirical mode decomposition, faster region-based convolutional neural network, Fourier transform, and Activation function

1. Introduction

The maternal structures and growth of fetal organs during gestation can be easily studied using the ultrasound imaging technique which is a low-cost and

non-invasive scanning procedure. This ultrasound scan is essential to monitor the mother and fetus for the assessment of fetal weight and, screening of abnormalities of the fetus and Doppler blood flow

measurement. Magnetic resonance imaging has the disadvantage that the image will be degraded due to the motion of the fetus. This degradation will be minimum when using the ultrasound scanning approach. The texture of fetal organs, morphology volume, and shape assessment will be helpful to access fetal health and pregnancy complication. Manual classification of Doppler scan images has high inter and intra-observer variability. Also, the single ultrasound examinations during the mid-trimester resulted in more than 20 images made the manual classification very tedious. Even though fetal ultrasound scan imaging has advantages like low cost, less harmful to both mother and fetus, it has the challenges such as low image quality, beam attenuation caused due by adipose tissue, low contrast, a low field of view. Also, there will be variations in the acquisition of fetal scan images such as variation due to gestational age, fetal position, and operator variability.

Recently artificial intelligence plays a crucial role in the classification system, especially the deep learning algorithms [1]. The convolutional neural network has a wide application in different medical image classification such as radiology [2], OCT (optical coherence tomography) [3], fundus images [4], MRI (Magnetic resonance imaging) images [5], and dermatology [6]. This CNN will be helpful in estimating complex patterns from the images where there is difficulty in detecting the RoI (region of interest) or in extracting the features from the RoI. The CNN algorithm [5] was used to classify the 13 fetal standard scan planes from the 30 minutes long video scan data. However, this system was trained using weakly supervised label data. Also, the video contains more additional surrounding data to the CNN that reduces the performance of this model. A conditional random field (CRF) is used [7] which can recognize the heart of the fetus in the frames of video. The fetus can also be detected using the random forest [8]. The fetal organs are then classified using the CNN (namely fetal body, fetal head, and non-fetal parts). However, this approach also uses additional clinical information such as fetal biometry plane position for detecting the body and head accurately. The CNN with multiple passes [9] and the iterative scheme are also used to identify the fetal brain images.

The authors Li et al. [10] classified the fetal tissue and the amniotic fluid using different pooling and convolutional structures. The accuracy of this approach in detecting the fetal body is 67%. Different authors worked in detecting the abnormality in the human brain. The authors Attallah et al. [11] used diagonal quadratic discriminates analysis, K-nearest neighbor, random forest and Naïve Bayes for classifying the brain scan image as normal or abnormal. The authors Sridar et al. [12] classified 14 fetal structures by extracting the local and global features. The authors Selvathi et al. [13] used different networks such as CNN, Google Net, and AlexNet for detecting the abnormality. The AlexNet model attains an accuracy of 90.43%. Congenital heart disease can also be detected by the fetal ultrasound images where the authors Sushma et al. [14] used the statistical features and support vector machine with a pattern classifier. The authors Sibio et al. [15] used an explainable residual learning approach for detecting the congenital heart disease of the fetus. This residual learning approach extracts discriminative features using the convolutional neural network from the cardiac anatomical structures of the fetus. This learning approach attains an accuracy of 93%.

The decomposition algorithms are also used to extract useful information from the medical images like singular value decomposition [16], wavelet decomposition is specifically designed to decompose the 2D images. Decomposition like empirical mode decomposition (EMD) [17] are widely used to decompose 1D signals like ECG, EEG, etc., which can be useful to detect the essential IMF (intrinsic mode function).

To reduce the intra and inter-observer variation in the classification of Doppler scan images and for the fast and accurate classification results an automatic fetal ultrasound scan image classification system is proposed. The contributions of the work are highlighted below:

- (i) The work uses the empirical mode decomposition to extract the essential global features from the 2D ultrasound fetal Doppler images where the EMD algorithm is applied from the 2 corner regions in a zig-zag diagonal pattern.

- (ii) The scheme also uses a faster RCNN with a dual sigmoid activation function, which improves the accuracy of classification in big data fetal Doppler scan image classification.
- (iii) The performance validation was done using the parameters such as accuracy, specificity, precision, sensitivity, F1 score, time complexity, and AUC on a huge dataset that contains 12,400 images.

The forthcoming sections of the paper are arranged as follows, Section 2 depicts the proposed ultrasound fetal

scan image classification system, Section 3 provides the experimental results and the analysis. Finally, the conclusion is provided in section 4.

2. Proposed method

Fig 1 presents the structure of the proposed Doppler scan image classification system, where the scan image $D(x, y)$ is preprocessed or scaled to a size of $M \times M$ to obtain the pre-processed image $d(x, y)$.

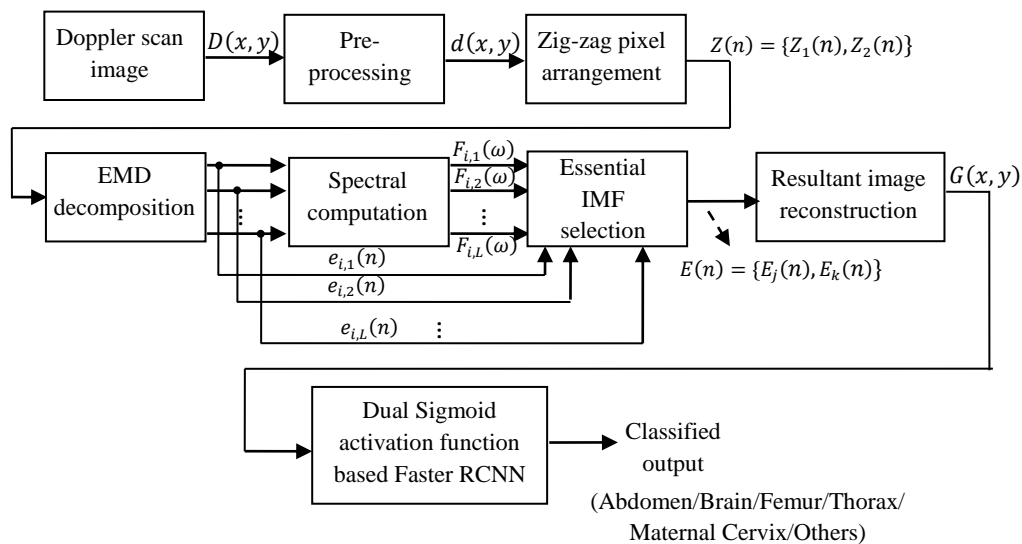


Fig 1: Block diagram of proposed Doppler scan image classification

Using the preprocessed image $d(x, y)$, the zigzag pixel sequence is constructed from top left to bottom right

$Z_1(n)$ and top right to bottom left $Z_2(n)$. Fig 2 depicts the zigzag pixel sequence construction from top left to bottom right.

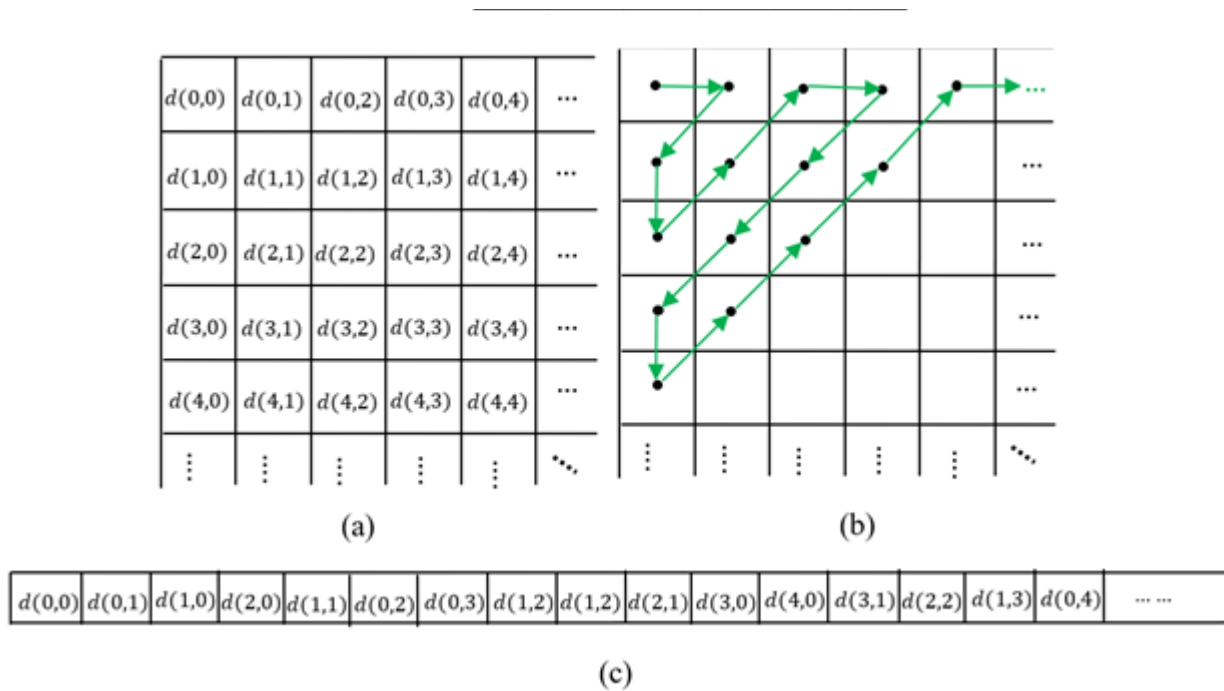


Fig 2: Construction of zig-zag pixels from the top left to bottom right (a) Pixel Coordinate representation (b) Zig-zag pixel formation (c) Zig-zag pixel sequence

2.1 EMD algorithm

The empirical mode decomposition algorithm [17] will decompose the sequence $Z_1(n)$ and $Z_2(n)$ to each L number of IMFs such that

$$Z_i(n) = \sum_{l=1}^L e_{i,l}(n) + R_i(n) \quad (1)$$

Where $i = 1$ and 2 . Here, $e_{i,l}(n)$ represents the IMF and $R_i(n)$ represents the residual of the i^{th} sequence. The EMD algorithm is presented below.

Algorithm 1:

Input: Number of IMF level L , the input sequence $Z_i(n)$.

Output: Decomposed IMFs $e_{i,l}(n)$ and residuals $R_i(n)$.

Step 1: Estimating the local maxima and minima.

Step 2: Estimate the lower envelope and upper envelope after connecting all the local minima and maxima by spline cubic interpolation.

Step 3: Calculate the mean $m_{i,l}$ from the upper and lower envelope.

Step 4: Calculate the difference between the signal $Z_i(n)$ and the mean $m_{i,l}$ represented as

$$H_{i,l} = Z_i(n) - m_{i,l} \quad (2)$$

Step 5: Check if $H_{i,l}$ is a valid IMF of $Z_i(n)$, then

$$e_{i,l} = H_{i,l} \quad (3)$$

Step 6: The residue can be estimated by the relation

$$Z_i(n) - e_{i,l} = r_{i,l} \quad (4)$$

Step 7: Treating $r_{i,l}$ as the original signal step 1 to 6 is repeated to obtain L number of IMFs

The zig-zag pixel sequence $Z_1(n)$ is decomposed using EMD with L levels. Let the decomposed IMFs be $e_{1,1}(n), e_{1,2}(n), \dots, e_{1,L}(n)$. Similarly the zig-zag pixel sequence $Z_2(n)$ is decomposed using EMD with L levels. Let the decomposed IMFs be $e_{2,1}(n), e_{2,2}(n), \dots, e_{2,L}(n)$.

Using the Fourier transform the spectrum of the IMFs are estimated using the relation

$$F_{i,l}(\omega) = FFT(e_{i,l}(n)) = \sum_{n=0}^{N-1} e_{i,l}(n)e^{-j\omega n}$$

$$l = 1, 2, \dots, L \text{ and } i = 1, 2 \quad (5)$$

here N is the number of FFT points. The T point moving average is accomplished on the Fourier domain $F_{i,l}(\omega)$. The N point moving average Fourier sequence be expressed as

$$\hat{F}_{i,l}(\omega) = \frac{1}{T} \left[\begin{array}{l} |F_{i,l}(\omega - \frac{T}{2})| + \\ |F_{i,l}(\omega - (\frac{T}{2} + 1))| + \dots + |F_{i,l}(\omega)| \\ + |F_{i,l}(\omega + 1)| + |F_{i,l}(\omega + 2)| \dots + |F_{i,l}(\omega + \frac{T}{2})| \end{array} \right] \quad (6)$$

$$\hat{F}_{i,l}(\omega) = \frac{1}{T} \sum_{p=-T/2}^{T/2} |F_{i,l}(\omega + p)| \quad (7)$$

The spectral averaging is performed on $\hat{F}_{i,l}(\omega)$

$$H_{i,l}(\omega) = \frac{1}{U} \sum_{\omega=0}^{U-1} \hat{F}_{i,l}(\omega) \quad (8)$$

Where U is the maximum frequency component present in $\hat{F}_{i,l}(\omega)$. The frequency index of the first spectral magnitude whose value is $0.5 \times H_{i,l}(\omega)$ is

estimated on $H_{i,l}(\omega)$. Let the frequency index on L number of IMF, be $\omega_{i,1}, \omega_{i,2}, \dots, \omega_{i,L}$. The frequency index is sorted in ascending order. Let the sorted frequency be $\hat{\omega}_{i,1}, \hat{\omega}_{i,2}, \dots, \hat{\omega}_{i,L}$. The IMF's whose frequency index is $\hat{\omega}_{i,1}$ and $\hat{\omega}_{i,L}$ are initially, chosen as the required mode. The frequency spacing is then estimated using the sorted frequency index.

$$\delta = \frac{1}{(L-1)} (\hat{\omega}_{i,L} - \hat{\omega}_{i,1}) \quad (9)$$

The required frequency index between $\hat{\omega}_{i,1}$ and $\hat{\omega}_{i,L}$ are selected based on the frequency spacing δ . A mode that corresponds to $\hat{\omega}_{i,j}$ is selected as the required mode if the difference between the preceding and succeeding index is greater than the 2δ .

$$\hat{\omega}_{i,l+1} - \hat{\omega}_{i,l-1} > 2\delta l = 2 \dots L - 1 \quad (10)$$

To make the selection of required modes easier the frequency spacing can be chosen as $\delta = \frac{1}{(L-1)}$ and the frequency $\hat{\omega}_{i,1}$ is treated as 0 and the $\hat{\omega}_{i,L}$ is treated as 1 and the remaining intermediate frequency is normalized between 0 and 1. Fig 3 depicts an example for the selection of required modes where the normalized frequencies are $\hat{\omega}_{i,1} = 0, \hat{\omega}_{i,2} = 0.1, \hat{\omega}_{i,3} = 0.28, \hat{\omega}_{i,4} = 0.44, \hat{\omega}_{i,5} = 0.8, \hat{\omega}_{i,6} = 0.9, \hat{\omega}_{i,7} = 1$ and frequency spacing $\delta = 0.1667$ as depicted in Fig 3(a). Initially, the modes that correspond to $\hat{\omega}_{i,1} = 0$ and $\hat{\omega}_{i,7} = 1$ is considered as the required mode as depicted in fig 3(b). The mode $\hat{\omega}_{i,2}$ is classified as required or non-essential mode using equation (10). Since equation (10) is not satisfied it is treated as a non-essential mode as shown in Fig 3(c). This process is done alternatively on lower frequency and higher frequency modes as shown in Fig 3(d) to 3(h).

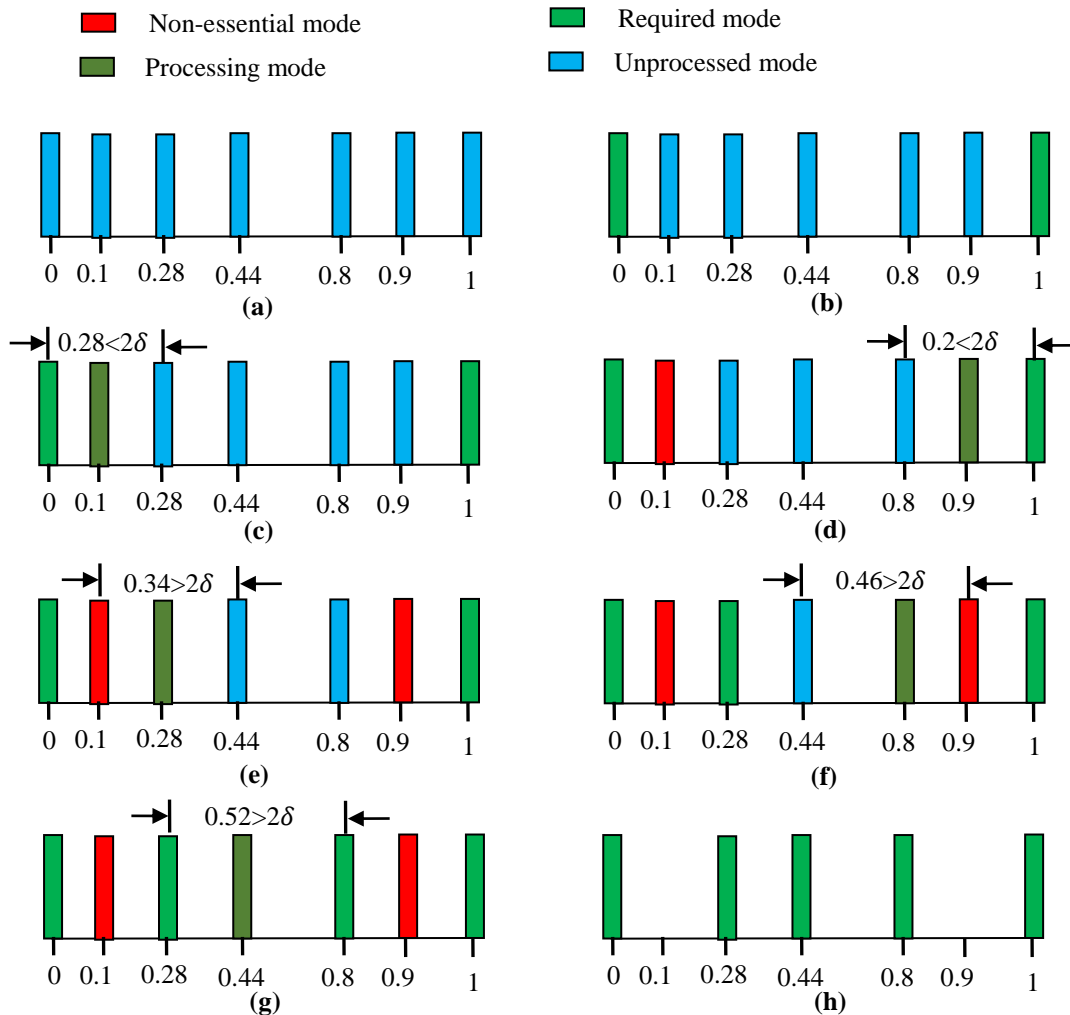


Fig 3: Selection of required modes

Let $E_j(n)$ and $E_k(n)$ represents the modes selected on the sequence $Z_1(n)$ and $Z_2(n)$ respectively. Where $j = 1, 2 \dots L_1$ and $k = 1, 2 \dots L_2$. Here L_1 and L_2 are

the number of modes that are selected in $Z_1(n)$ and $Z_2(n)$ respectively. The modes are $E_j(n)$ and $E_k(n)$ are summed and inverse zig-zag is applied to construct the resultant image $G(x, y)$.

2.2 Dual sigmoid activation based faster RCNN

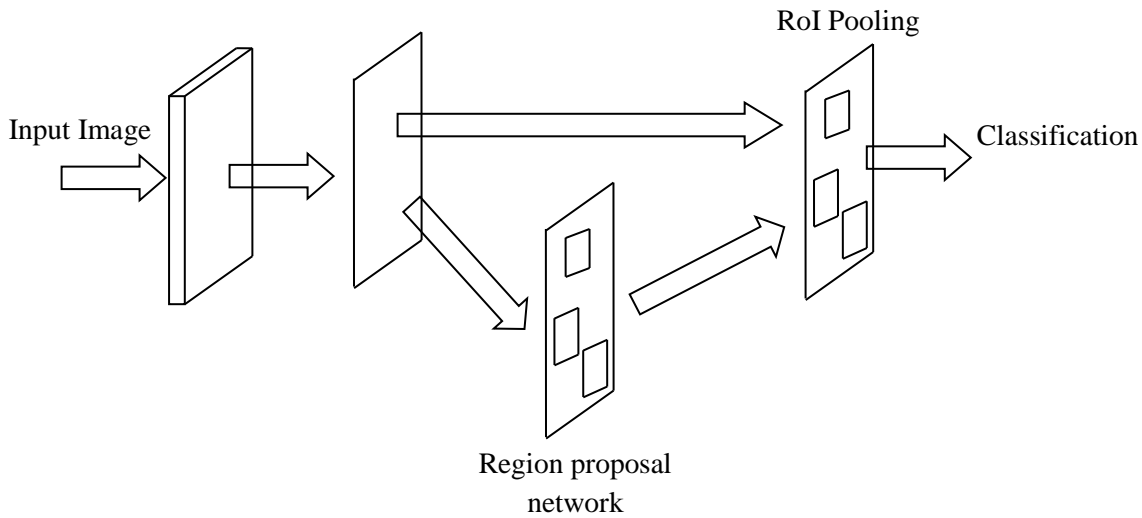


Fig 4: Block diagram representation of faster-RCNN

Both R-CNN and fast R-CNN run on CPU computation, where the faster RCNN [18] uses a convolutional network termed for generating the region proposals. The Faster R-CNN is a mixture of Fast R-CNN and RPN. The representation of faster R-CNN is depicted in fig 4. Instead of using the traditional sigmoid based activation function in a faster-RCNN network, the proposed approach introduces dual sigmoid function given by

$$G(x) = \frac{1}{1+e^{-x}} \quad (11)$$

The output of sigmoid activation lies between 0 and 1 and it is a Sshaped curve. The dual sigmoid activation has two Sshaped curves. The one S shaped curve corresponds to a positive x value, while the other corresponds to a negative x values. The function is expressed as,

$$G(x) = G_1(x) + G_2(x) \quad (12)$$

$$G(x) = \frac{1}{1+e^{-\varepsilon(x+\Delta)}} - 1 + \frac{1}{1+e^{-\varepsilon(x-\Delta)}} \quad (13)$$

The dual sigmoid function varies between -1 to 1.

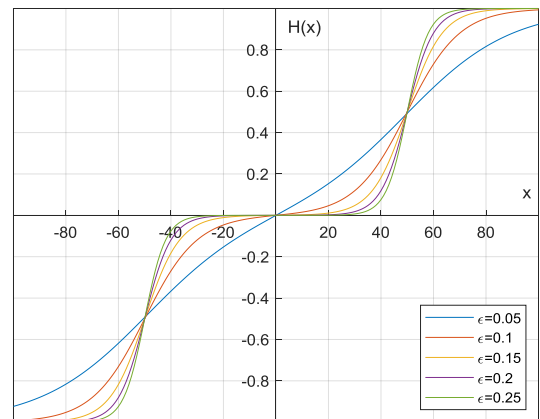


Fig 5: Activation function for various values of ε

Fig 5 shows the activation function for various values of ε , here $\Delta=100$. For lower values of ε the activation function is more linear, while for higher values of ε leads to an S-shaped curve or step-like function.

3. Experimental Results

The evaluation of the ultrasound scan image classification system was done with the fetal ultrasound datasets, which contains the scan images of 1792 patients. Therefore the dataset contains 12,400 images with six categories of images namely Maternal cervix, Thorax, Femur, Brain, Abdomen, and other regions. From 12,400

images 7129 randomly selected images are provided for training the classifier and the rest of the 5271 images are used for validation. The evaluation was done using the metrics such as sensitivity, specificity, precision, accuracy, and F1 score which is mathematically expressed as,

$$Sensitivity = \frac{T_{pos}}{(T_{pos}+F_{neg})} \quad (14)$$

$$Specificity = \frac{T_{neg}}{(T_{neg}+F_{pos})} \quad (15)$$

$$Accuracy = \frac{T_{pos}+T_{neg}}{(T_{pos}+T_{neg}+F_{pos}+F_{neg})} \quad (16)$$

$$Precision = \frac{T_{pos}}{(T_{pos}+F_{pos})} \quad (17)$$

$$F1\ Score = \frac{2 \times (precision \times sensitivity)}{precision + sensitivity} \quad (18)$$

The sample image from the ultrasound dataset for each category is depicted in Fig 6. The proposed method uses the number of modes as $L = 8$ and the faster RCNN implementation as provided in [18]. However, the activation function was replaced by the dual sigmoid activation function with $\epsilon = 0.2$.

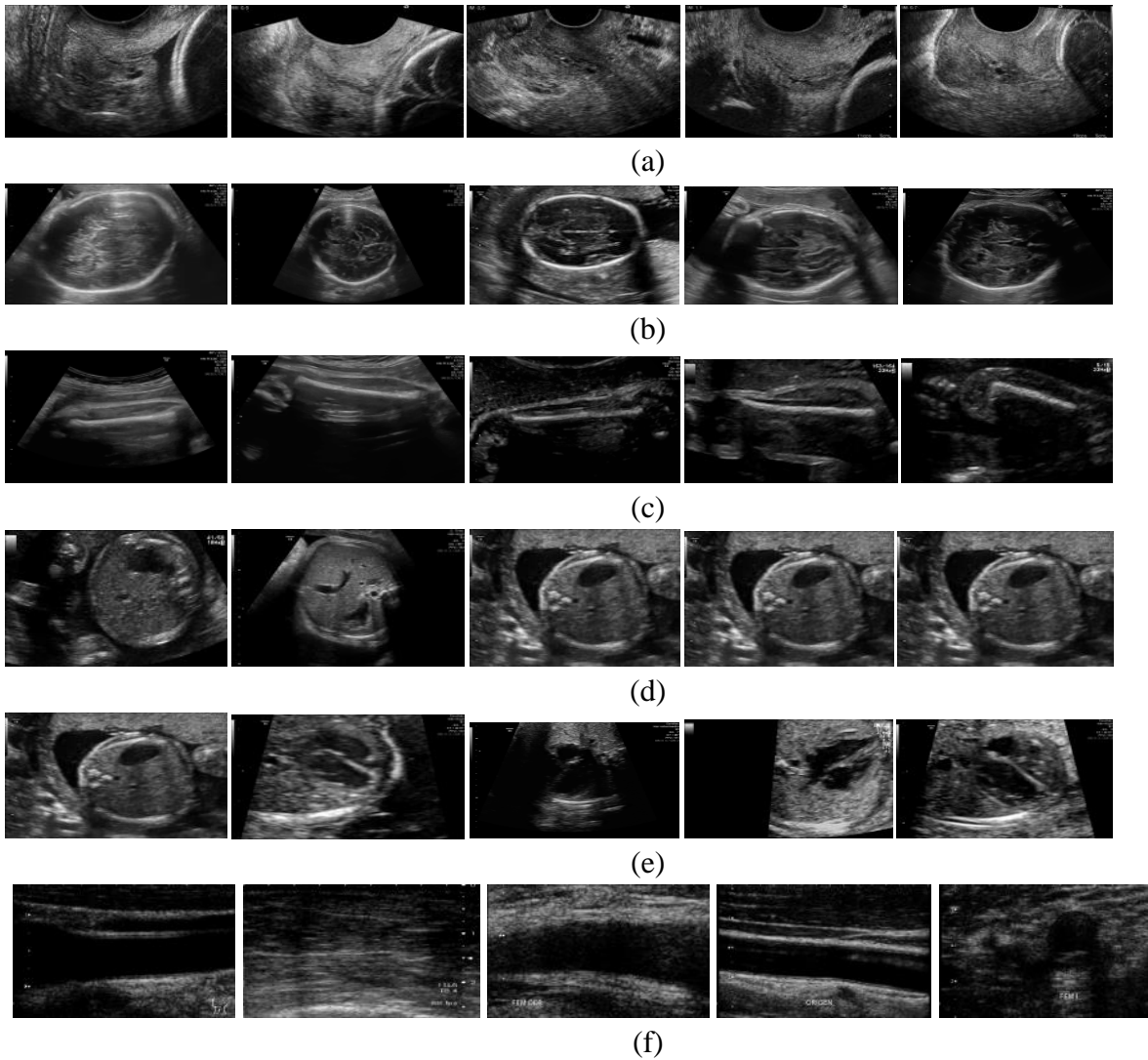


Fig 6: Sample images from the fetal ultrasound Doppler scan images (a) Maternal Cervix (b) Fetal brain (c) Fetal femur (d) Fetal Abdomen (e) Fetal thorax (f) Others

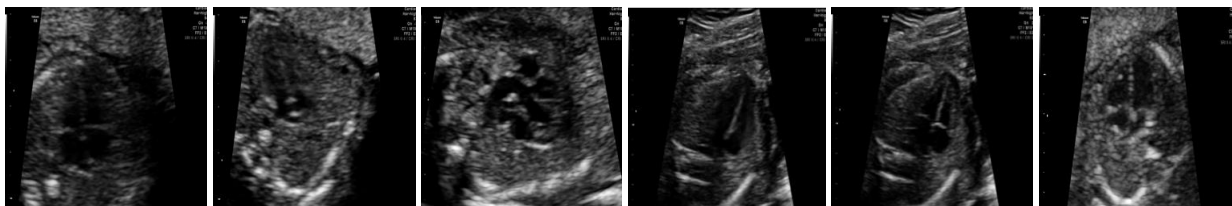
Table 1: Comparison of the proposed approach with other traditional approaches based on accuracy, precision, sensitivity, specificity, and F1-score.

Schemes	Accuracy (%)	Precision (%)	Sensitivity (%)	Specificity (%)	F1-Score (%)
VGG	92.1 ± 6.1	88.64	89.16	92.48	90.16
MobileNet	87.5 ± 9.6	89.07	90.45	92.01	90.87
Inception-v3	93.5 ± 5.0	90.47	91.11	93.69	93.28
ResNet-152	92.8 ± 5.5	91.99	90.32	95.05	93.71
ResneXt-101	94.0 ± 4.8	90.56	92.89	94.21	91.73
SE-ResNeXt-101	92.7 ± 5.8	92.23	93.01	96.11	91.89
DenseNet-169	93.6 ± 5.1	93.01	93.66	97.56	92.45
Proposed	94.78 ± 3.48	93.32	94.73	98.94	93.96

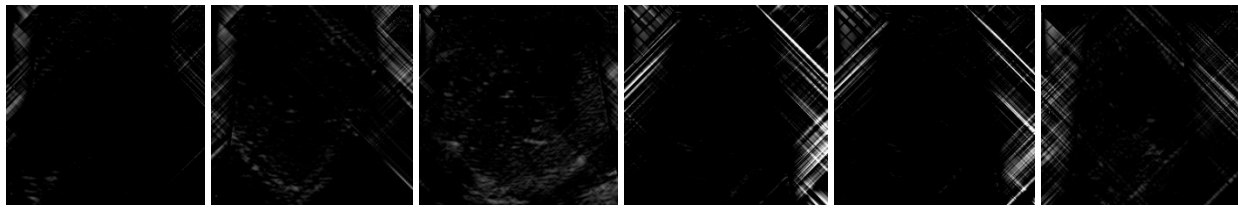
The proposed method was also compared with other deep learning models namely VGG [19], MobileNet [20], Inception-v3 [21], ResNet-152 [22], ResneXt-101 [23], SE-ResNeXT-101 [24] and DenseNet-169 [25]. Table 1 depicts the comparison of our method with the state-of-the-art deep learning models. The proposed scheme provides a accuracy, specificity, precision, sensitivity, and F1-score of 94.78%, 98.94%, 93.32%, 94.73%, and 93.96% respectively which is higher than the DenseNet-160 model. The proposed method shows a 1.18%, 1.07%, 0.31%, 1.38% and 1.51% improvement in

accuracy, sensitivity, precision, specificity and F1-score than the DenseNet-169 approach.

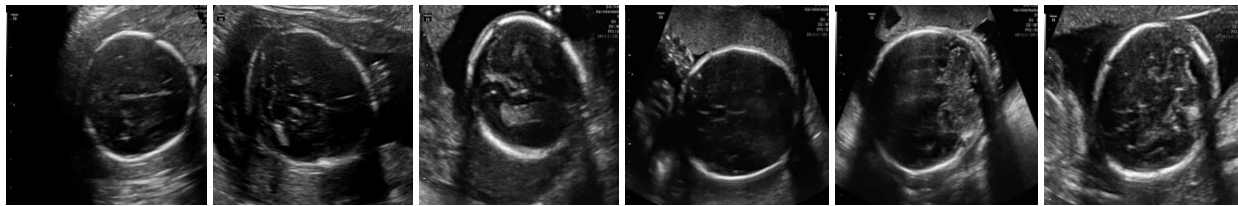
The global features extracted by the EMD algorithm for the fetal thorax and fetal brain scan image are presented in Fig 7. The global features that are extracted by the EMD algorithm for the fetal femur and fetal abdomen scan image are depicted in Fig 8. Fig 9 depicts the global features extracted by the EMD algorithm on maternal cervix images and other image categories.



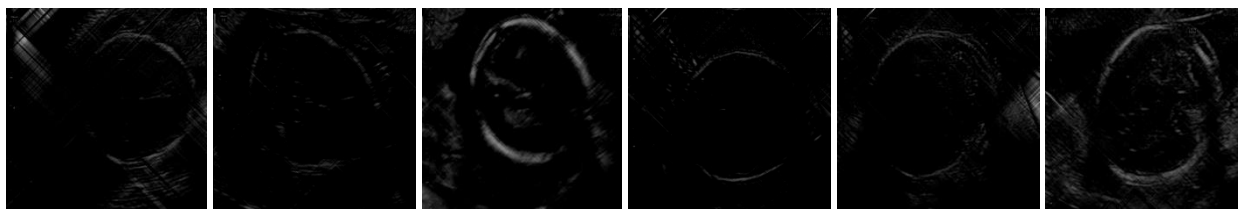
(a)



(b)

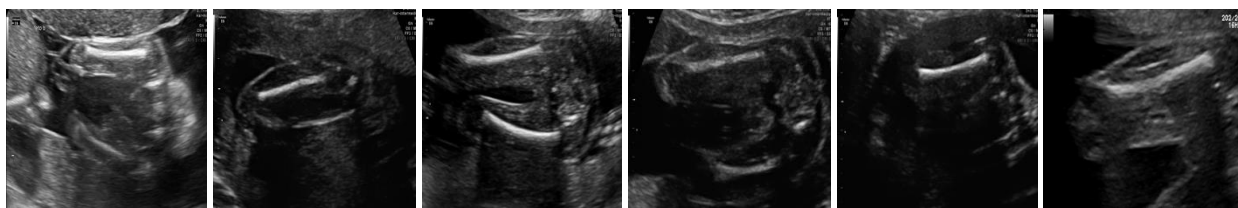


(c)

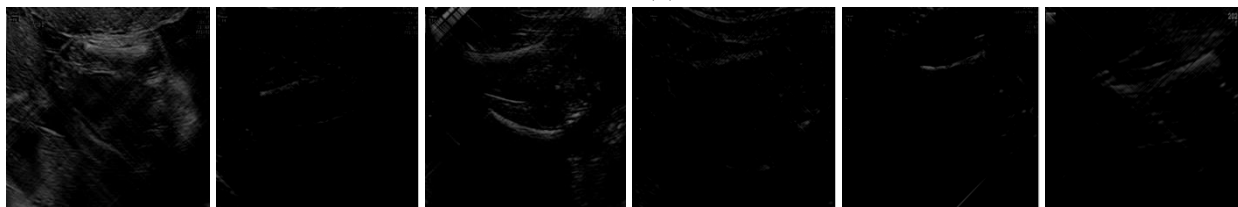


(d)

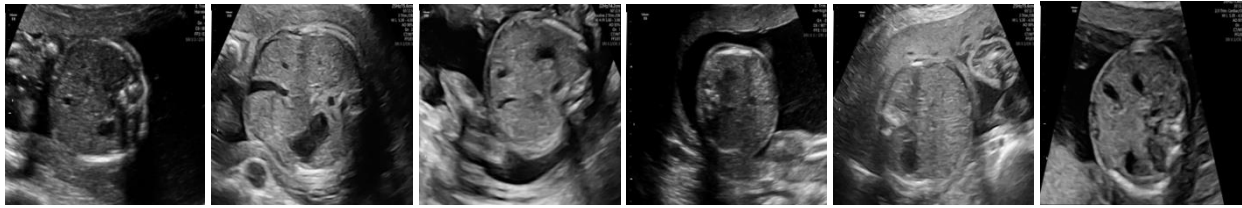
Fig 7: Representation of EMD features (a) Input Fetal thorax images (b) EMD features for Fetal thorax images (c) Input Fetal brain images (d) EMD features for Fetal brain images



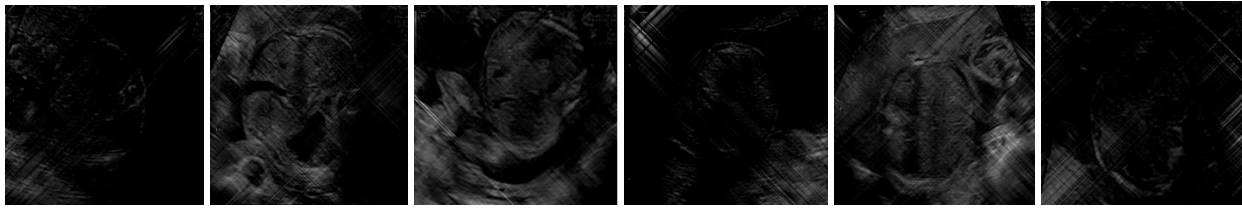
(a)



(b)

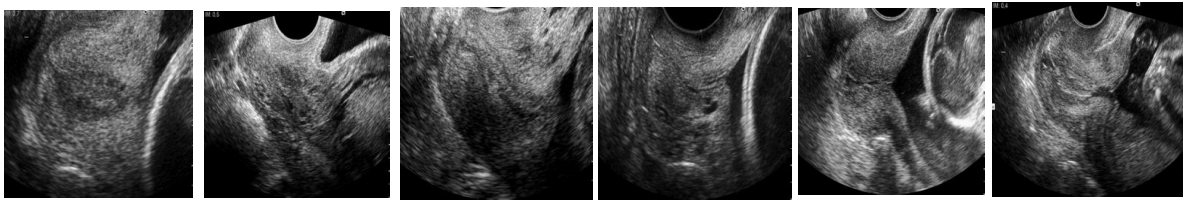


(c)

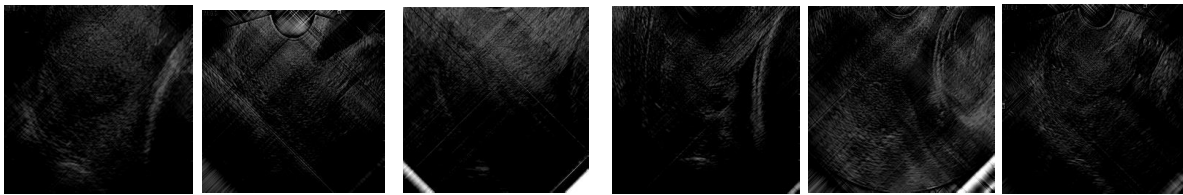


(d)

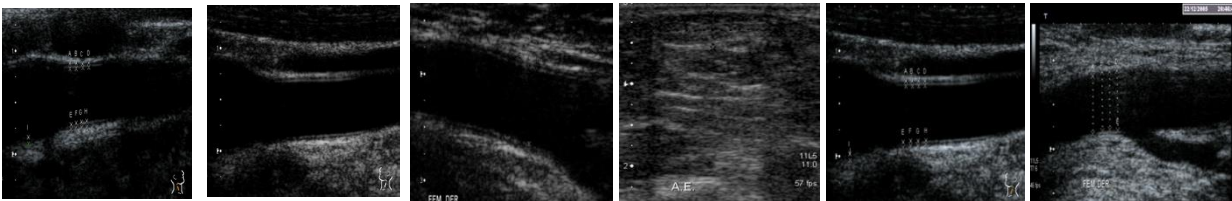
Fig 8: Representation of EMD features (a) Input Fetal femur images (b) EMD features for Fetal femur images (c) Input Fetal abdomen images (d) EMD features for Fetal abdomen images



(a)



(b)



(c)

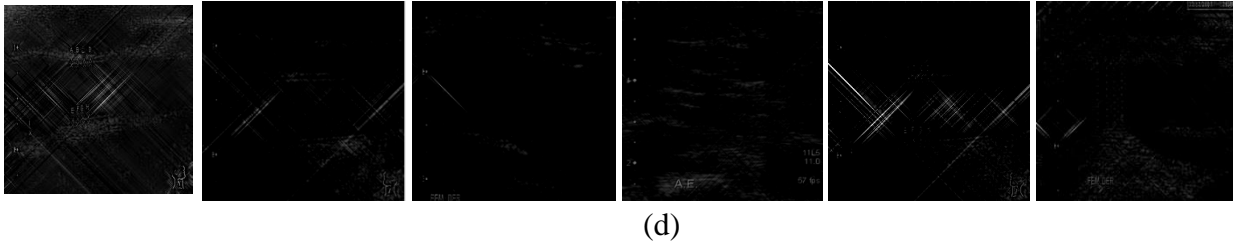


Fig 9: Representation of EMD features (a) Input Fetal maternal cervix images (b) EMD features for maternal cervix images (c) Input other image categories (d) EMD features for other image categories

Fig 10 shows the validation confusion matrix with 5271 images and Fig 11 illustrates the graphical comparison of accuracy, precision, sensitivity, specificity, and F1-score for the proposed approach with the state-of-the-art

approaches. The accuracy is higher than the ResNeXt-101, where the precision, specificity, and sensitivity were higher than the DenseNet-169 and the F1-score is higher than the ResNet-152 model.

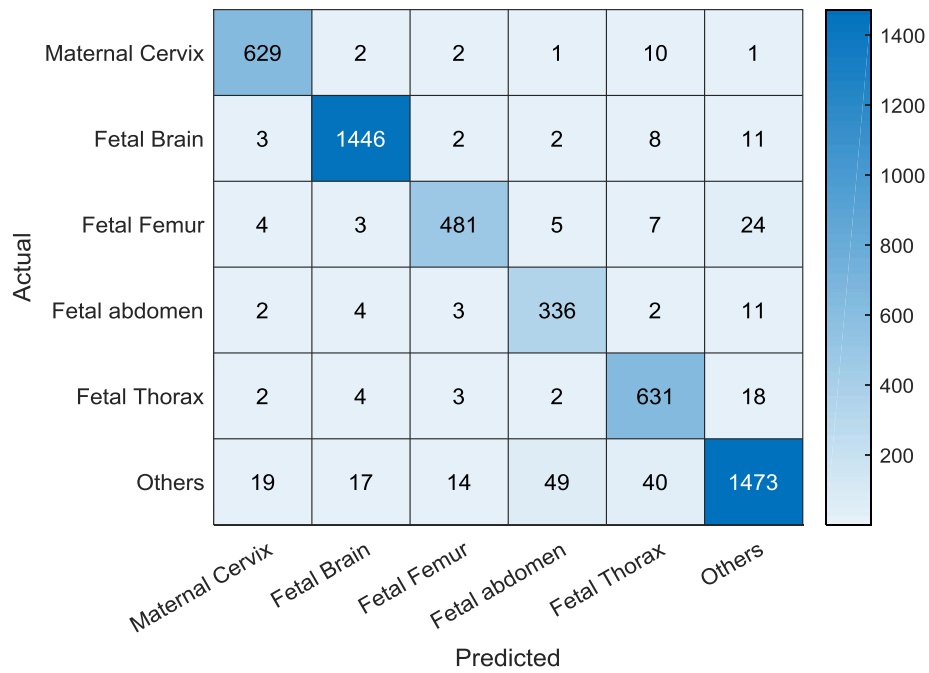


Fig 10: Confusion matrix obtained for the proposed method with $L = 8$

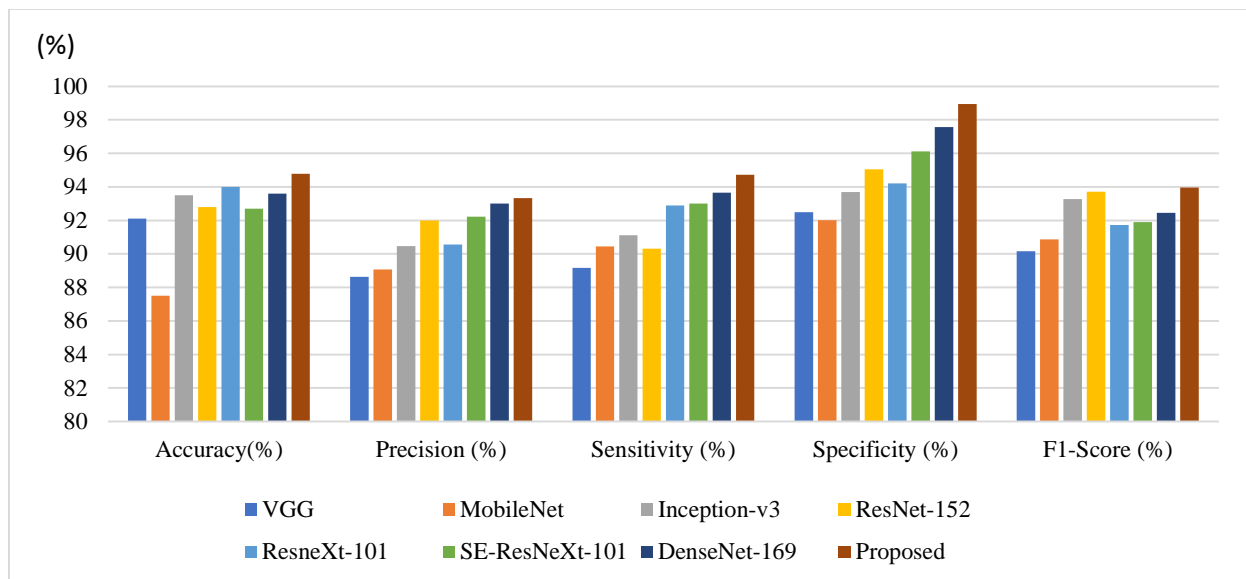


Fig 11: Graphical comparison of our method with other models with respect to the accuracy, specificity, precision, sensitivity, and F1-Score

Table 2: Comparison of Accuracy and time complexity for different values of L

L	Accuracy (%)	Time of training (s)	Time of classification (s)
3	88.14	5,046	0.49
4	90.36	5,256	0.62
5	92.11	5,491	0.73
6	93.8	5,702	0.82
7	94.13	5,914	0.91
8	94.78	6,126	0.99
9	94.6	6,392	1.08
10	94.27	6,602	1.13

Table 2 shows the comparison of accuracy, time of training, and time of classification for different values of L. The time complexity in training and classification increases as the number of IMFs to be decomposed gets increases. As the value of L increases, the accuracy also increases till L = 8. Further increase in value of L, the

accuracy starts reducing. Therefore the proposed system shows a better performance for L = 8. For L = 8, the proposed scheme provides an accuracy of 94.78%. Also, the time of training and time of classification of L = 8 is 6,126s and 0.99s respectively.

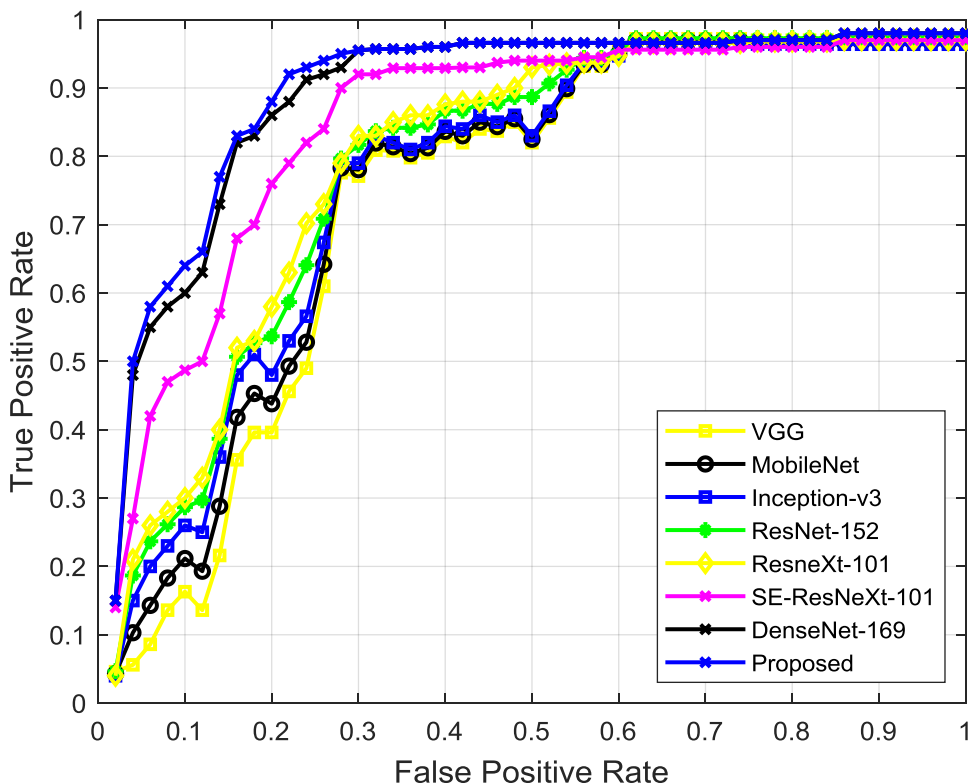


Fig 12: ROC comparison of our scheme with different deep learning models

Fig 12 depicts the ROC comparison of our scheme with the other schemes. The proposed method gives a higher AUC (area under the ROC curve) when compared to other traditional methods. The scheme provides an AUC of 0.9132. The forthcoming section depicts the conclusion of the work.

4. Conclusion

This paper introduced an ultrasound Doppler fetal scan image classification algorithm on big data that uses the EMD algorithm and the faster RCNN algorithm. The method initially preprocesses the image and decomposes the scan images to L number of IMFs. A required number of IMFs are used to construct the features. The EMD extracted features are trained using the faster RCNN algorithm. Instead of using the traditional activation layer, the proposed approach uses a dual sigmoid activation layer that improves the classification performance of the model in ultrasound scan image classification. A huge dataset that contains 12,400

images is used to validate the fetal scan image classification system performance with the metrics parameters namely accuracy, specificity, precision, sensitivity, and F1-score. The proposed method provides an F1-score, specificity, sensitivity, precision, and accuracy of 93.96%, 93.32%, 98.94%, 94.73%, and 94.78% respectively.

References

- [1]LeCun, Y., Bengio, Y. & Hinton, G. Deep learning. *Nat.* **521**, 436–444 (2015).
- [2]Hosny, A., Parmar, C., Quackenbush, J., Schwartz, L. H. & Aerts, H. J. Artificial intelligence in radiology. *Nat. Rev. Cancer* **18**, 500 (2018).
- [3] Das, Sraddha, et al. "Deep learning architecture based on segmented fundus image features for classification of diabetic retinopathy." *Biomedical Signal Processing and Control* 68 (2021): 102600.

- [4] Suchetha, M., Rajiv Raman, and Edwin Dhas. "Region of Interest based Predictive Algorithm for Subretinal Hemorrhage Detection using Faster R-CNN." (2021).
- [5] Litjens, G. *et al.* A survey on deep learning in medical image analysis. *Med. image analysis* 42, 60–88 (2017).
- [6] Esteva, A. *et al.* Dermatologist-level classification of skin cancer with deep neural networks. *Nat.* 542, 115 (2017).
- [7] Maraci, M., Bridge, C., Napolitano, R., Papageorghiou, A. & Noble, J. A framework for analysis of linear ultrasound videos to detect fetal presentation and heartbeat. *Med. Image Analysis* 37, 22–36 (2017).
- [8] Ryou, H. *et al.* Automated 3d ultrasound biometry planes extraction for first trimester fetal assessment. In *Machine Learning in Medical Imaging*, 196–204 (2016).
- [9] Li, Y. *et al.* Standard plane detection in 3d fetal ultrasound using an iterative transformation network. *Medical Image Computing and Computer Assisted Intervention – MICCAI 2018*, 392–400 (2018).
- [10] Lee, LokHin, Yuan Gao, and J. Alison Noble. "Principled Ultrasound Data Augmentation for Classification of Standard Planes." *International Conference on Information Processing in Medical Imaging*. Springer, Cham, 2021.
- [11] Attallah, Omneya, Maha A. Sharkas, and Heba Gadelkarim. "Fetal brain abnormality classification from MRI images of different gestational age." *Brain sciences* 9.9 (2019): 231.
- [12] Sridar, Pradeeba, et al. "Decision fusion-based fetal ultrasound image plane classification using convolutional neural networks." *Ultrasound in medicine & biology* 45.5 (2019): 1259-1273.
- [13] Xie, H. N., et al. "Using deep- learning algorithms to classify fetal brain ultrasound images as normal or abnormal." *Ultrasound in Obstetrics & Gynecology* 56.4 (2020): 579-587.
- [14] Sushma, T. V., et al. "Classification of Fetal Heart Ultrasound Images for the Detection of CHD." *Innovative Data Communication Technologies and Application*. Springer, Singapore, 2021. 489-505.
- [15] Qiao, Sibao, et al. "RLDS: An explainable residual learning diagnosis system for fetal congenital heart disease." *Future Generation Computer Systems* 128 (2022): 205-218.
- [16] Subba, Basant, and Prakriti Gupta. "A tdfvectorizer and singular value decomposition based host intrusion detection system framework for detecting anomalous system processes." *Computers & Security* 100 (2021): 102084.
- [17] Dubey, Rahul, et al. "Automated diagnosis of muscle diseases from EMG signals using empirical mode decomposition based method." *Biomedical Signal Processing and Control* 71 (2022): 103098.
- [18] Gonzales-Martínez, Rosa, et al. "Hyperparameters Tuning of Faster R-CNN Deep Learning Transfer for Persistent Object Detection in Radar Images." *IEEE Latin America Transactions* 20.4 (2022): 677-685.
- [19] Simonyan, K. & Zisserman, A. Very deep convolutional networks for large-scale image recognition. *CoRR abs/1409.1556* (2014).
- [20] Sandler, M., Howard, A., Zhu, M., Zhmoginov, A. & Chen, L.-C. Mobilenetv2: Inverted residuals and linear bottlenecks. *CVPR*(2018).
- [21] Szegedy, C. *et al.* Going deeper with convolutions. *CoRR abs/1409.4842* (2014).
- [22] He, K., Zhang, X., Ren, S. & Sun, J. Deep residual learning for image recognition. *CoRR abs/1512.03385* (2015).
- [23] Xie, S., Girshick, R., Dollar, P., Tu, Z. & He, K. Aggregated residual transformations for deep neural networks. In *Proceedings of the IEEE Conference on Computer Vision and Pattern Recognition*, 1492–1500 (2017).
- [24] Hu, J., Shen, L. & Sun, G. Squeeze-and-excitation networks. *CoRR abs/1709.01507* (2017).
- [25] Burgos-Artizzu, Xavier P., et al. "Evaluation of deep convolutional neural networks for automatic classification of common maternal fetal ultrasound planes." *Scientific Reports* 10.1 (2020): 1-12.